



Insights into rapid photodynamic inactivation mechanism of *Staphylococcus aureus* via rational design of multifunctional nitrogen-rich carbon-coated bismuth/cobalt nanoparticles

Rong Wang, Bowen Zhang, Zichen Liang, Yixin He, Zonghan Wang, Xingfa Ma, Xiaolin Yao, Jian Sun, Jianlong Wang*

College of Food Science and Engineering, Northwest A&F University, Yangling, 712100, Shaanxi, China

ARTICLE INFO

Keywords:

g-C₃N₄
Mott-Schottky
Photodynamic inactivation
Mechanism
Wound healing

ABSTRACT

Despite the development of various drugs and materials, bacterial infections remain a serious problem for wound healing. Most current materials cannot simultaneously provide antibacterial effects, reusability, and biocompatibility, and participate in stimulating cellular behaviour to promote bacterial wound healing. Herein, multifunctional nitrogen-rich carbon-coated bismuth/cobalt nanoparticles (Bi@Co@CN) with foam-like structures synthesised by a simple two-step method showed remarkably improved magnetic and photoconversion effects. These are promising candidates as photodynamic inactivation materials. Within 20 min, > 99.999% *Staphylococcus aureus* (*S. aureus*) were killed by the composite due to its strong ability to generate reactive oxygen species (ROS) and thermal energy under simulated visible light. Additionally, Bi@Co@CN also displayed high stability: its antibacterial efficiency underwent rapid photodynamic inactivation over five cycles. *In vitro* results revealed that ROS and photothermal conversion of materials can seriously damage bacterial cell membranes and inhibit the virulence factors produced by bacteria, which ultimately leads to the death of *S. aureus*. Moreover, *in vivo* assessment of wound healing showed that the material was very effective for bacteria-accompanied wound healing and did not cause detectable damage to the major organs. Therefore, the Bi@Co@CN composite has great potential as a safe multimodal treatment system for active photodynamic inactivation and wound healing.

1. Introduction

Contagious diseases caused by bacteria are one of the most important health worldwide, afflicting millions of people every year [1,2]. Methicillin-resistant *Staphylococcus aureus* (MRSA) in particular poses a serious social health threat [3]. To date, various drugs and materials have been developed, such as metal ions [4–6], antibiotics [7,8] and antimicrobial peptides [9] to inhibit or reduce the growth of harmful bacteria. Nevertheless, these materials are associated with high cost, antibiotic resistance, environmental pollution, and complex chemical processes. Green chemistry may be the best route to a sustainable and environmentally friendly antibacterial agent.

Graphitic carbon nitride (g-C₃N₄), a metal-free polymeric semiconductor with a narrow bandgap, is an alternative antibacterial agent because it creates fewer disinfection by-products, is easy to use, is effective against antibiotic-resistant strains, and can harvest abundant solar energy [10–12]. The main reactive species involved in the

photocatalytic activity of semiconductor materials are reactive oxygen species (ROS), such as superoxide radicals ($\cdot\text{O}_2^-$), hydroxyl radicals ($\cdot\text{OH}$), and hydrogen peroxide (H₂O₂) [13,14]. The energy created by electron-hole pairs enables g-C₃N₄ to generate ROS for photodynamic inactivation applications [15–17]. Unfortunately, the rapid recombination of these electron-hole pairs is a major barrier to achieving high-efficiency solar energy conversion and greatly limits its practical application. Therefore, various strategies are utilized to limit recombination, such as by forming heterostructures [18–20], decorating with metal nanoparticles [21,22], and synthesising hollow nanospheres [23]. Among these strategies, decoration of metal nanoparticles on the g-C₃N₄ surface is of particular interest as it can form a Schottky barrier. This barrier helps charge transfer between the semiconductor and the metal, and substantially facilitates electron-hole separation. When the metal and g-C₃N₄ are in close contact, the different work functions of the two components and the Fermi-level result in the formation of Schottky barriers and space charge regions at the metal-g-C₃N₄

* Corresponding author.

E-mail address: wanglong79@nwsuaf.edu.cn (J. Wang).

<https://doi.org/10.1016/j.apcatb.2018.09.030>

Received 1 June 2018; Received in revised form 29 August 2018; Accepted 11 September 2018

Available online 15 September 2018

0926-3373/ © 2018 Elsevier B.V. All rights reserved.

interface [24–27]. This charging effect can be strong and may promote the activity of metal particles in photocatalytic reactions.

Among metal particles, some inexpensive metals with adjustable structure and chemical stability have proven to be suitable candidates for photocatalysis. Bismuth (Bi), a semiconductor, could be an ideal substitute for noble metals due to its bandgap energy, low cost, and biocompatibility [28–31]. First, its narrow bandgap means that Bi-based photocatalysts can harvest visible light to achieve highly efficient disinfection [32,33]. Second, the introduction of metallic Bi on the surface of $g\text{-C}_3\text{N}_4$ can establish a Schottky barrier at the interface, which facilitates charge transfer between semiconductors and metals, and significantly accelerates electron-hole separation [34–36]. Therefore, enhanced photocatalytic performance is achieved by the decoration of metallic Bi on the $g\text{-C}_3\text{N}_4$ surface. Additionally, it is necessary, yet difficult, to separate used nanomaterials from a disinfection system to avoid secondary pollution and recycled nanomaterials. Cobalt (Co) magnetic separation may be the most efficient route as it can not only enhance photothermal conversion ability, but also provide an additional magnetically-targeted function [37,38]. Therefore, the strategy of combining $g\text{-C}_3\text{N}_4$ with both Bi and Co components could improve photocatalytic and photothermal performances.

In this study, we constructed nitrogen-rich carbon-coated Bi/Co nanoparticles (Bi@Co@CN) using a simple thermal condensation method, and demonstrated their outstanding photodynamic inactivation of *S. aureus* for the first time (Scheme 1a). This material exhibited a greater photodynamic inactivation than other advanced antibacterial materials reported to date. The inactivation effect of Bi@Co@CN toward *S. aureus* was investigated using a standard plate-counting method under visible-light irradiation ($\lambda > 420\text{ nm}$) provided by a xenon lamp. Electron paramagnetic resonance (ESR) and scavenger experiments were conducted to investigate the major ROS in the photodynamic inactivation process. Fluorescence-based live/dead testing of cells, measurements of intracellular ATP and membrane potential, and scanning electron microscopy (SEM) observations were used to provide mechanistic insight into bacterial destruction. Additionally, *in vivo*

experiments for wound healing were conducted to assess the biocompatibility of Bi@Co@CN in wound infection (Scheme 1b). The outstanding properties associated with Bi@Co@CN suggested that these types of materials could be used as efficient light-harvesting catalysts for photodynamic inactivation.

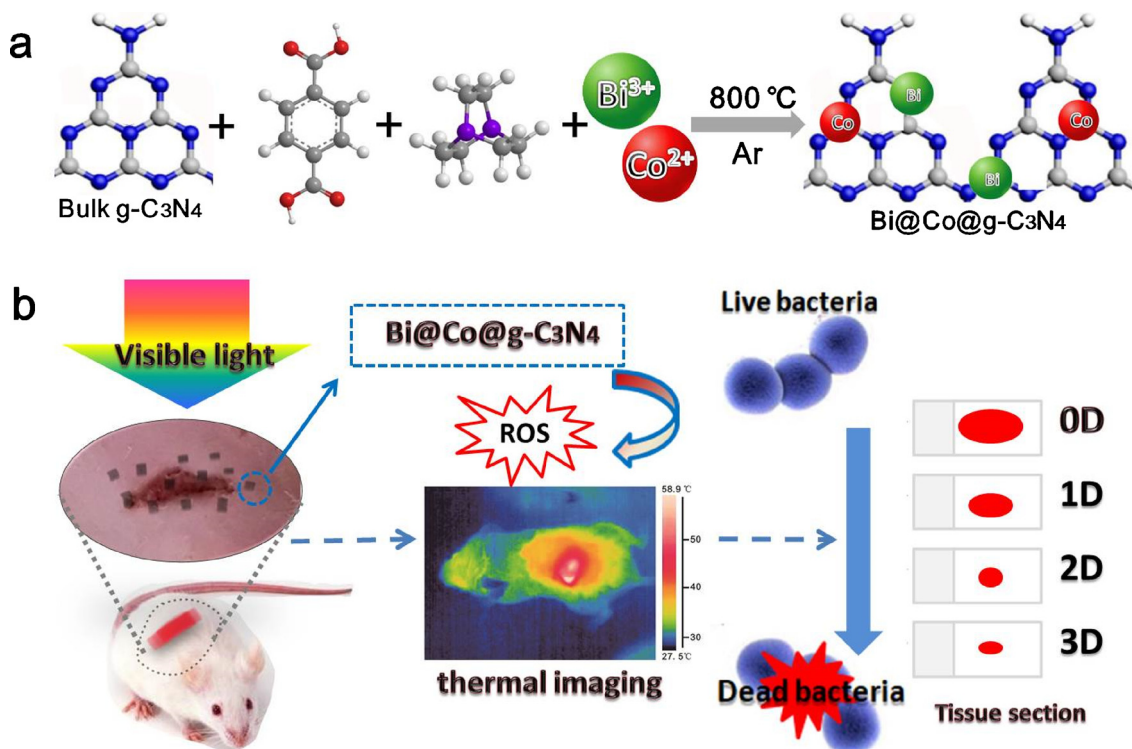
2. Experimental section

2.1. Materials

Silver nitrate was purchased from kermel Chemical Reagent Co., Ltd (Tianjin China), sodium oxalate, 1,4-benzenedicarboxylic acid and triethylene diamine were purchased from Aladdin chemistry Co. Ltd. (Shanghai, China), 2,2,6,6-Tetramethylpiperidine (TEMPOL), ethylenediaminetetraacetic acid disodium salt (Na_2EDTA), propidium iodide (PI) and fluorescein isothiocyanate (FITC) were obtained from Sigma-Aldrich (Sigma-Aldrich, Shanghai, China), urea was purchased from Beijing Solarbio Science & Technology Co., Ltd (Beijing, China), *N,N*-Dimethylformamide (DMF), ammonium hydroxide, isopropanol and anhydrous ethanol (EtOH, AR) were purchased from Kelong Chemical Reagent Co., Ltd. (Chengdu, China), bismuth nitrate was obtained from Xiya Chemical Reagent Co., Ltd (Shandong China), $\text{DiBAC}_4(3)$ was purchased from ATT Bioquest (Sunnyvale, USA). The water used in all experiments was de-ionized (DI). All of the chemical reagents of analytical grade were used as received without further purification.

2.2. Synthesis of the $\text{Bi@Co@g-C}_3\text{N}_4$ (Bi@Co@CN)

Graphitic carbon nitride ($g\text{-C}_3\text{N}_4$) were synthesized according to our previous work [17]. First, 130 mg of $\text{Co}(\text{NO}_3)_2 \cdot 6\text{H}_2\text{O}$ and $\text{Bi}(\text{NO}_3)_3 \cdot 5\text{H}_2\text{O}$ were initially added into 50 mL of dimethylformamide (DMF) to prepare a transparent solution. After vigorous stirring for 10 min, 302 mg of 1,4-benzenedicarboxylic acid and 216 mg of triethylene diamine were added into the mixed solution, followed by 60 min stirring. Then 2.06 g of $g\text{-C}_3\text{N}_4$ was added to the mixed DMF



Scheme 1. (a) Schematic illustration of the fabrication of Bi@Co@CN nanocomposites. (b) Schematic of Bi@Co@CN with generation of reactive oxygen species (ROS) and thermal energy enhancing the photodynamic inactivation under visible-light irradiation.

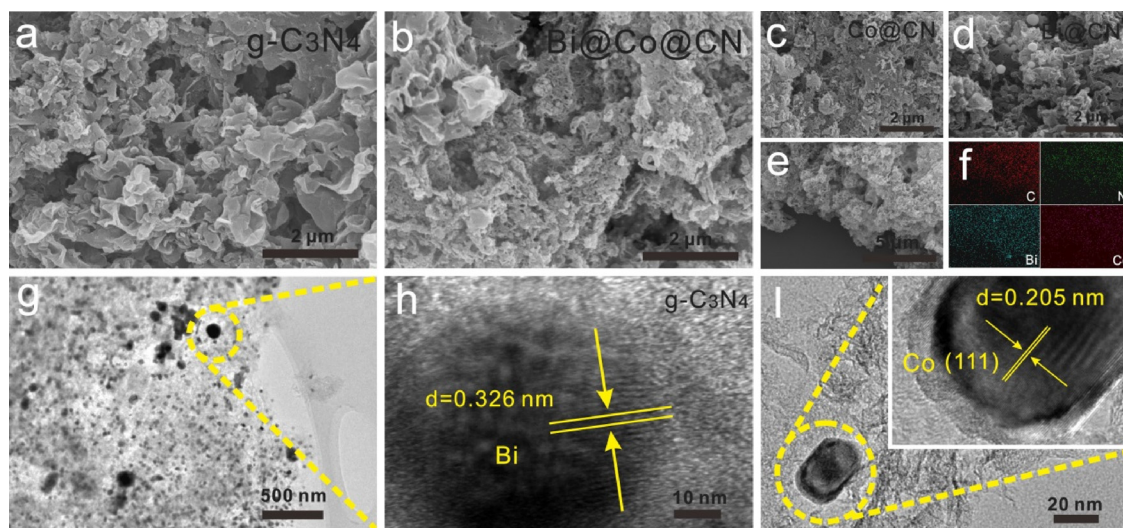


Fig. 1. (a) SEM image of urea-derived g-C₃N₄. (b) SEM image of Bi@Co@CN. (c) SEM image of Co@CN. (d) SEM image of Bi@CN. (e) SEM image of Bi@Co@CN for EDS. (f) The corresponding elemental mappings of C, N, Bi and Co elements in Fig. 1e. (g) HRTEM image of Bi@Co@CN. (h) HRTEM image of Bi@Co@CN for Bi nanoparticles. (i) HRTEM image of Bi@Co@CN for Co nanoparticles.

solution under 3 h magnetic stirring. After solvent was removed, the green solid powder was transferred to a quartz boat, heated over 8 h to 800 °C in air under an Ar atmosphere and maintained at this temperature for 1 h. The as-obtained black samples were used for further characterizations and photocatalytic reactions.

2.3. Characterization

Scanning electron microscopy (SEM) and energy-dispersive spectroscopy (EDS) analysis were conducted by S-4800 FE-SEM (Hitachi, Japan). High-resolution transmission electron microscopy (HRTEM) images were taken on FEI Electron optics GZF2.0 electron microscope at an acceleration voltage of 200 kV. The X-ray diffraction (XRD) patterns were utilizing a Bruker D8 diffractometer with high-intensity Cu-K α in the 2 θ range of 10–70°. X-ray photoelectron spectroscopy (XPS) data was conducted by Axis Ultra DLD X-ray photoelectron spectrometer. The fluorescent-based cell live/dead tests and microscopic fluorescence images for skin tissues were harvested using a laser scanning confocal microscopy (Nikon A1+/A1R+, Japan). ESR signals of spin-trapped paramagnetic species were recorded by using a JEOL JES-FA200 electron spin resonance spectrometer. The time-resolved fluorescence emission spectra were recorded at room temperature with a fluorescence spectrophotometer (FLS1000, Edinburgh Instruments). All pH measurements were performed with a PB-10 digital pH-meter (Sartorius, Germany) with a combined glass-calomel electrode.

2.4. Photocatalytic disinfection tests

The disinfection tests of Bi@CN, Co@CN and Bi@Co@CN were evaluated via the inactivation of *Staphylococcus aureus* (ATCC 29213) and methicillin-resistant *Staphylococcus aureus* (MRSA), which were received from Prof. Yang and Prof. Wang (College of Food Science and Engineering, Northwest A&F University), respectively. Before the microbiological experiments, all the glasswares and the culture medium solution were autoclaved for 30 min at 121 °C. First, bacterial cells were incubated in nutrient solution at 37 °C for 18 h and then centrifuged to remove metabolites. The bacterial solution was then diluted with phosphate buffer solution (PBS, 0.01 M, pH 7.4) to obtain ca. 10⁷ colony forming units per milliliter (CFU/mL). For each antibacterial experiment, 2 mg catalyst powders and 10 mL of *S. aureus* suspension were pipetted into a container. Then, the antibacterial experiment was irradiated by a commercial 300 W xenon lamp PLS-SXE300UV (Beijing

Perfectlight Technology Ltd, China) equipped with an optical cutoff filter ($\lambda > 420$ nm), which could eliminate ultraviolet light. In addition, the average power energy density of the irradiation was about 100 mW cm⁻² (1 sun illumination) measured by PL-MW2000 spectroradiometer (Beijing Perfectlight Technology Ltd, China). At given irradiation time interval (0, 5, 10, 15, 20, 30 min), 100 μ L of tested suspension samples were spread on freshly LB agar plates, and the colonies were counted to confirm the survival bacterial numbers after incubation for 24 h at a temperature of 37 °C. Control experiments (*S. aureus* without catalyst under illumination and *S. aureus* with catalyst in dark) were also performed.

3. Results and discussion

3.1. Synthesis and characterisation of Bi@Co@CN

To enable Bi@Co@CN materials for possible use as photocatalysts, we developed a thermal condensation method using the Bi(NO₃)₃ and Co(NO₃)₂ metal salts, and low cost organic molecules as the precursors. The graphite carbonitride, is then used as a main nitrogen source for forming a nitrogen-enriched carbon support added to a mixed solution of metal salts and organic molecules in dimethylformamide (DMF). The solid mixture obtained after removal of the solvent is carbonized in an Ar atmosphere at 800 °C. The obtained black powder was used for further characterization. Fig. 1a shows the morphology of pristine g-C₃N₄ (CN), which displayed a two-dimensional structure consisting of small, wrinkled, flat sheets. Thermal decomposition of metal salts on the surface of g-C₃N₄ particles could explain the formation of a foam-like structure of Bi@Co@g-C₃N₄ (Bi@Co@CN), as revealed by SEM (Fig. 1b). We also examined the carbonisation products of the metallic Bi and Co analogues. Fig. 1c–d shows that carbonisation at 800 °C of Co@g-C₃N₄ (Co@CN) and Bi@g-C₃N₄ (Bi@CN) did not significantly change their morphologies; both displayed a foam-like morphology. Fig. 1e–f are representative images of Bi@Co@CN from energy-dispersive X-ray spectroscopy (EDS) elemental mapping for C, N, Bi, and Co. This mapping clearly shows that Bi and Co were highly dispersed in the composite, which confirmed its synthesis. Moreover, high-resolution transmission electron microscopy (HR-TEM) of Bi@Co@CN revealed Bi nanoparticles and Co nanoparticles (Fig. 1g–i). The images show many metal particles decorated on the surface of g-C₃N₄ nanosheets compared with the pristine g-C₃N₄ (Fig. S1). Additionally, the HR-TEM images reveal the highly integrated nanostructure of the

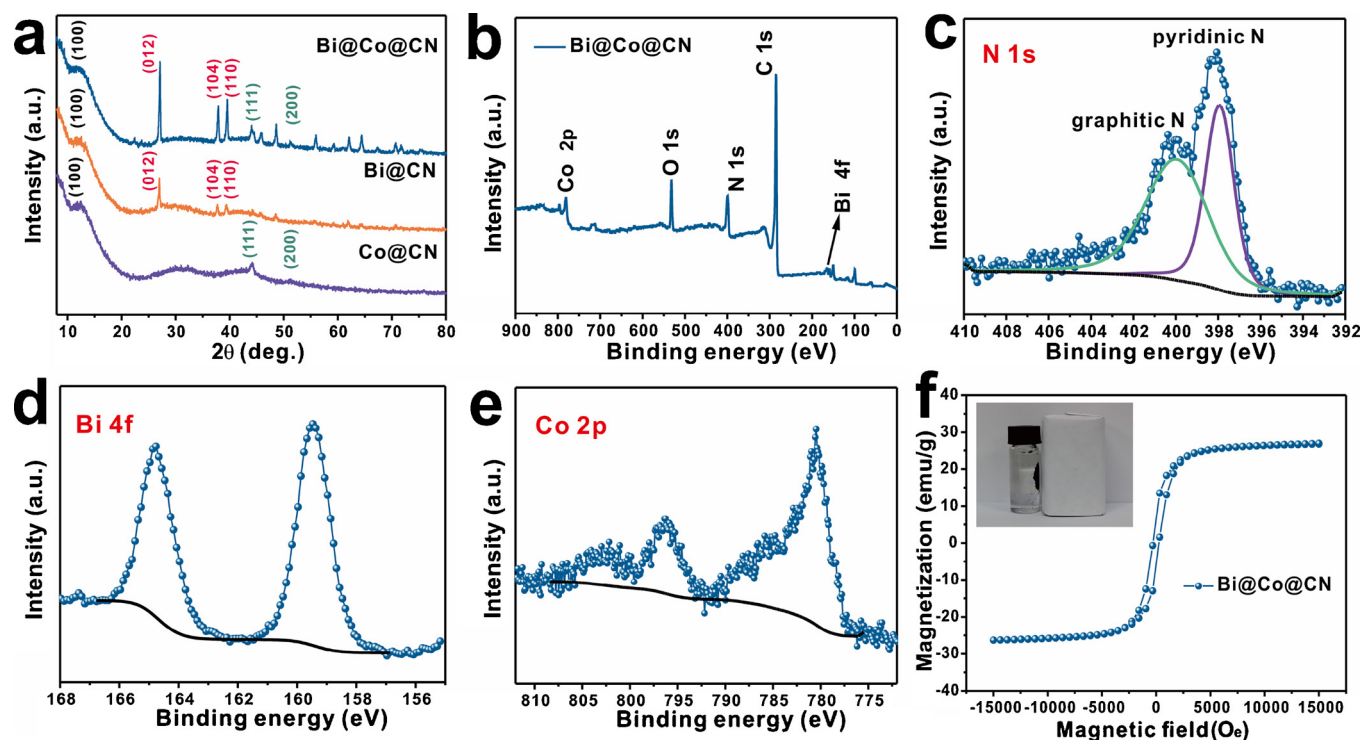


Fig. 2. (a) XRD patterns of Co@CN, Bi@CN and Bi@Co@CN. (b) XPS spectra of Bi@Co@CN. (c) High-resolution N 1s XPS spectra of Bi@Co@CN. (d) High-resolution Bi 4f XPS spectra of Bi@Co@CN. (e) High-resolution Co 2p XPS spectra of Bi@Co@CN. (f) Magnetization curve of Bi@Co@CN.

layered carbon-coated Bi and Co nanoparticles (Fig. 1g). The lattice plane spacing of metallic Bi is 0.326 nm, corresponding to the (012) planes (Fig. 1h) [24]. An additional lattice spacing of 0.205 nm was observed (Fig. 1i), which was attributed to the (111) plane of metallic Co [22]. The carbon layer acts as a shell to protect the metal nanoparticles from aggregation, and significantly enhances their charge separation capability, which is beneficial to photocatalysis.

X-ray diffraction (XRD) measurements were performed to identify the crystalline phases and structures of the composites. Fig. 2a shows that all of the composites displayed a distinct peak corresponding to the (100) plane at ca. 13.1°. This peak was attributed to an in-plane structural packing motif, consistent with the graphitic-like layered structure of g-C₃N₄. For Co@CN (purple curve), the two peaks were in good agreement with the (111) and (200) peaks reported for metallic Co. For Bi@CN (orange curve), the characteristic peak of Bi (JCPDS PDF 44-1246) confirmed the presence of a Bi-metallic rhombohedral phase in the Bi@CN composite. All of the diffraction peaks for Bi and Co were observed for Bi@Co@CN (blue curve), revealing the formation of metallic Bi, Co, and graphitic carbon. X-ray photoelectron spectroscopy (XPS) measurements further confirmed the elemental compositions and chemical states of the prepared samples. Fig. 2b displays the survey scan spectra of the Bi@Co@CN composite. Peaks for Bi, Co, C, N, and O are evident, indicating the successful synthesis of Bi@Co@CN. Fig. 2c shows the high-resolution N 1s XPS spectrum of Bi@Co@CN. Peaks at 397.9 and 399.9 eV were assigned to pyridinic N and graphitic N, respectively. The peaks centred at 159.5 and 164.8 eV are typical of Bi – Bi bonds found in elemental Bi (Fig. 2d). The high-resolution O 1s XPS spectrum (Fig. S2) showed peaks centred at 532.2 eV, which were attributed to oxygen-containing species, further excluding the presence of a significant amount of Co oxide surface layer (which would appear at 529.2 eV) in the Bi@Co@CN sample. The broad Co 2p peak (Fig. 2e) suggested the presence of Co–N bonds in the sample. The slight shift of the peak (Fig. S3) to higher energy indicated that introduction of metallic Bi caused a decrease in the electron density of Co particles compared with Co@CN. This observation supports the important role of the Mott–Schottky effect at the heterojunction interface in changing the

electron density, which affected the photocatalytic activity of Bi@Co@CN [22,26]. The spectra of Co@CN and Bi@CN are also presented in Fig. S4. Fig. 2f shows the magnetisation curve with a hysteresis loop. The saturation magnetisation of the Bi@Co@CN was ca. 28 emu/g, demonstrating its good magnetic signal that is suitable for magnetic separation. The introduction of Co enhanced the photothermal conversion ability and facilitated the separation and recovery of the photocatalyst.

3.2. Disinfection activity in vitro under visible-light irradiation

Staphylococcus aureus (ATCC29213) was selected to study the antibacterial ability of the prepared composites because it is responsible for a wide range of serious diseases, including skin and soft tissue infections [39,40]. The disinfection performance was evaluated by mixing the *S. aureus* suspension and the prepared photocatalyst under different time intervals (0, 5, 10, 15, 20, and 30 min). Fig. 3a compares the cell density of Bi@Co@CN, Co@CN, and Bi@CN toward *S. aureus*. Negligible antimicrobial activity was observed in the dark and light controls, indicating that both illumination and the photocatalysts had almost no effect on *S. aureus*. Disinfection efficiency was significantly improved under visible-light irradiation compared with in the dark. Over a period of 20 min of visible-light irradiation, Co@CN and Bi@CN displayed very low disinfection efficiencies, and the quantities of viable bacteria were ca. 4.0 log₁₀ cfu/mL and 4.9 log₁₀ cfu/mL, respectively. In contrast, the quantity of viable bacteria toward Bi@Co@CN could reach 2.1 log₁₀ cfu/mL after 20 min of irradiation, which was significantly better than that found for Co@CN and Bi@CN. Furthermore, Bi@Co@CN showed a 7-log inactivation of bacterial concentration (> 99.999% inactivation efficiency) and no live bacteria were detected after 30 min of visible-light illumination. This was caused by the excellent charge separation efficiency between the metal nanoparticles and the g-C₃N₄ nanostructures. To investigate the effects of foam like structure for the enhanced antibacterial activity, we explored the antibacterial activity of materials before carbonization and after carbonization. As shown in Fig. S5a, Bi@Co@CN (before carbonization)

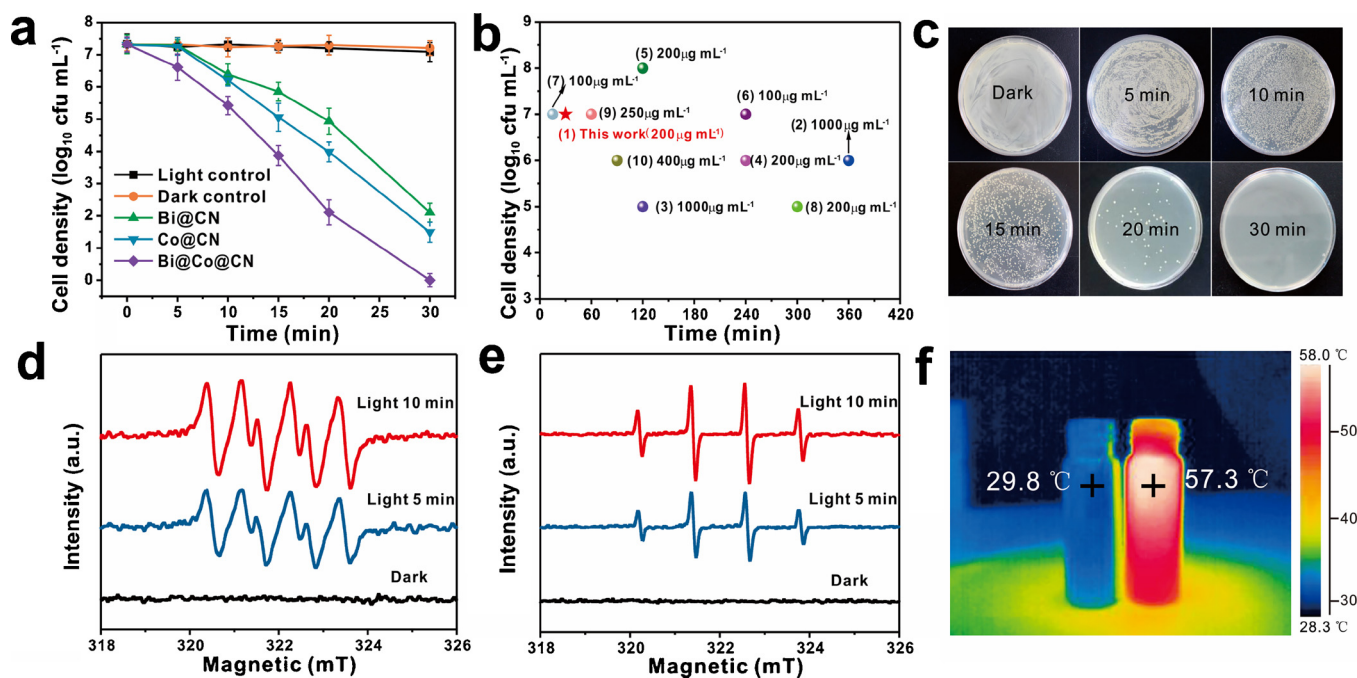


Fig. 3. (a) Cell density of different samples against *S. aureus* under visible-light irradiation. (b) Disinfection-performance comparison of with the literature values of other photocatalysts. (c) Bacterial colony growth in the presence of Bi@Co@CN under different irradiation time. (d) ESR spectra for $\cdot\text{O}_2^-$ in the presence of Bi@Co@CN suspension. (e) ESR spectra for $\cdot\text{OH}$ in the presence of Bi@Co@CN suspension. (f) Thermal image of Bi@Co@CN under visible-light irradiation.

displayed a low disinfection efficiency compared with Bi@Co@CN, indicating that the foam like structure of the composite is important for the enhanced antibacterial activity. The higher surface areas of Bi@Co@CN (Fig. S5b) can serve as more efficient transport route and provide more adsorption site in the photocatalytic reaction process, matching with its enhanced antibacterial efficiency [41–43]. In addition, the antibacterial activities of Bi@Co@CN toward Gram-negative bacteria (*E. coli* ATCC25922 and *Salmonella* LT2) were conducted to verify the board-spectrum antibacterial activity. As shown in Fig. S6, our materials also have a good bactericidal effect on Gram-negative bacteria, indicating that the Bi@Co@CN composites have a board-spectrum antibacterial activity under visible light irradiation. For further comparison of antibacterial activity, we reviewed numerous photocatalytic inactivation studies and compared the disinfection performances of those photocatalysts (Fig. 3b and Supplementary Table S1). Our Bi@Co@CN composite exhibited superior disinfection than most reported photocatalysts. As Table S1 showed, 7-log inactivation of *S. aureus* was obtained after treating Bi@Co@CN for 30 min with a concentration of $200\ \mu\text{g mL}^{-1}$, which was ca. eight times faster than with Ni-TiO₂ (240 min). These results clearly indicate that the synthesised Bi@Co@CN exhibited faster photodynamic inactivation. To clarify the experimental results, Fig. 3c displays the number of bacterial colonies grown in the presence of Bi@Co@CN against *S. aureus* at various irradiation times (dark, 5, 10, 15, 20, and 30 min) on agar plates. The images show that adding the catalysts caused a gradual killing of the bacteria with increasing illumination time.

ROS, such as hole (h^+), electron (e^-), hydroxyl radical ($\cdot\text{OH}$), superoxide radical ($\cdot\text{O}_2^-$), and H_2O_2 , have been reported as the main reactive species in the photocatalytic activity of semiconductors. They also have excellent antibacterial properties. However, it is not clear which of these ROS played a major role in the photocatalytic process; therefore, various scavengers were utilized to determine the exact roles. Fig. S7 shows that a significant inhibitory effect of bacterial inactivation was observed after the addition of the TEMPOL and isopropanol radical scavengers. This proved that the $\cdot\text{O}_2^-$ and $\cdot\text{OH}$ species were important in the photocatalytic process. Electron spin resonance (ESR) spectra of the as-prepared material were recorded for confirmation. Fig. 3d shows

that no $\cdot\text{O}_2^-$ was produced by the Bi@Co@CN catalyst in the dark, whereas the nearly 1:1:1:1 quartet pattern characteristic of $\cdot\text{O}_2^-$ captured by the DMPO radical scavenger was observed after irradiation for a few minutes in the presence of Bi@Co@CN. In addition to superoxide radical, hydroxyl radical is another important ROS. Under visible-light irradiation, the characteristic peak for $\cdot\text{OH}$ with an intensity ratio of 1:2:2:1 was observed (Fig. 3e), which confirmed the generation of $\cdot\text{OH}$ radicals toward Bi@Co@CN under visible-light irradiation. Furthermore, as a plasmonic metal, Bi nanoparticles will concentrate incident photon energy into plasmon oscillations, which could conspicuously enhance the visible-light harvesting and the charge separation [44–47]. To prove the plasmon effect of Bi metal in photodynamic activity, ns-level time-resolved fluorescence decay spectra was conducted. As shown in Fig. S8 and Table S2, with an emission wavelength of 442 nm, the average fluorescence lifetimes of g-C₃N₄ (carbonization) and Bi@CN were 2.4087 and 2.6374 ns, respectively. The average carrier lifetime of Bi@CN was prolonged compared to g-C₃N₄. This result indicated the SPR effect of Bi metal will contribute to charge separation, thus enhancing visible light photocatalytic performance. These findings above demonstrated that $\cdot\text{OH}$ and $\cdot\text{O}_2^-$ were produced by irradiated Bi@Co@CN suspension, providing solid proof that photogenerated holes and electrons were efficiently separated and reacted with adsorbed oxygen/ H_2O to produce abundant of ROS, which finally induced the disinfection of bacteria. Additionally, the temperature during disinfection experiments was measured because heat is vital for bacterial survival under irradiation. The temperature changes in the study were measured with a thermal imager. Fig. 3f shows that $200\ \mu\text{g mL}^{-1}$ Bi@Co@CN (right bottle) increased the temperature to above 57.3 °C compared with the minimal temperature gain achieved with the photocatalysts (left bottle) during 30 min of irradiation. This illustrates the excellent photothermal conversion efficiency with the introduction of metallic nanoparticles. The contributions of photocatalytic and photothermal effects were shown in Fig. S9. Moreover, cycling runs of Bi@Co@CN were conducted to study its photocatalytic stability. Fig. S10a shows that the Bi@Co@CN photocatalyst could be reused at least four times with only a slightly decreased disinfection activity, which was attributed to the inevitable mass loss of materials after

centrifugation. These results are consistent with previous literature that the loss of activity was mainly ascribed to mass loss in the recycling process [48,49]. To investigate the performance reduction trend after four cycles, the fifth cycle was conducted. As shown in Fig. S10a, the quantity of viable bacteria toward Bi@Co@CN could reach $3.5 \log_{10}$ cfu/mL after 30 min of irradiation even after the fifth cycle. The XRD patterns of Bi@Co@CN before and after photocatalysis show that its structure remained almost unchanged (Fig. S10b). These combined results indicate that Bi@Co@CN has rapid photodynamic inactivation performance and can remain intact after recycling several times.

3.3. Mechanistic insight into bacterial destruction

Based on the above studies, we concluded that the mechanism for the highly improved photodynamic inactivation of Bi@Co@CN involved effective separation of photoexcited charges and excellent photothermal conversion efficiency, which promoted inactivation by the abundant generation of ROS and thermal energy. To further investigate the mechanism underlying the inactivation performance of Bi@Co@CN toward *S. aureus*, fluorescence-based live/dead tests of bacterial cells were carried out to verify the integrity of bacterial cell membranes (Fig. 4). The cells were stained with FITC and PI fluorescent nucleic acid dyes. FITC passes through the unbroken membrane of live bacterial cells and stains fluorescent green, while PI is a cell-impermeable stain with red fluorescence that labels only dead cells [50,51]. Fig. 4 shows that there were few dead cells in the dark control experiment, while after 30 min of irradiation treatment with Bi@Co@CN photocatalysts, the bacterial cells exhibited a stronger red fluorescence compared with the control. This suggested that the cell membranes of *S. aureus* were severely damaged during the disinfection process. This discovery prompted us to investigate the membrane potential of *S. aureus*. A membrane potential-sensitive fluorochrome, DiBAC₄(3), was used to investigate the changes of cell membrane. This fluorescent dye is a member of a class of sensitive probes that respond to depolarizing cells and bind to intracellular proteins or membranes to enhance fluorescence. Increased depolarisation increases the inflow of anionic dyes and increases fluorescence. In contrast, hyperpolarisation is manifested as a decrease in fluorescence [52,53]. Fig. 5a shows that bacteria treated with Bi@CN, Co@CN and Bi@Co@CN performed cell membrane hyperpolarisation under visible-light-driven irradiation, as

revealed by a significantly decrease in relative fluorescence. Additionally, the membrane potential steadily decreased with increasing irradiation time, indicating the good photocatalytic sterilisation performance of Bi@Co@CN. This hyperpolarization may be due to ROS directly attacking the bacterial cell membrane, resulting in positively charged ions moving from the cytoplasm to the extracellular [54]. The results are consistent with ROS directly acting on the cell membrane, causing cell hyperpolarisation. Additionally, ATP plays an important role in the antibacterial process as it can be used in many cell functions, including the transport of substances across cell membranes. In prokaryotes, the cell membrane is important for cell energy conversion and for processing nutrients, synthesising structural macromolecules, and secreting enzymes [55]. The results show that the intracellular ATP concentration of *S. aureus* ATCC 29,213 decreased rapidly when photocatalysts were added under visible-light irradiation, indicating the disruption of bacteria cells (Fig. 5b). The decrease of intracellular ATP may be due to the photothermal effect and changes in cell membrane permeability, which would lead to ATP leakage. The damage to the cell membrane motivates us to investigate bacterial contents, such as total protein, which could be detected during the inactivation process. Fig. 5c shows that the total protein increased with increasing irradiation time; this behaviour was in good agreement with the inactivation results. The above results indicate that the reactive oxygen species and thermal energy, which were generated by Bi@Co@CN under irradiation, attacked the bacterial cells and released the total protein.

The damage process to bacterial cells induced by the Bi@Co@CN composite was further investigated. The structure and morphological changes of *S. aureus* were studied using SEM at different time intervals (Fig. 5d–i). Fig. 5d shows an SEM image of *S. aureus* before photocatalytic sterilisation, in which well-preserved cell membrane are clearly observed with interior evenly colored and well arrangement of the bacteria. After 5 min of irradiation in contact with Bi@Co@CN, the bacterial cells adhered to the material and the cell membrane began to wrinkle (Fig. 5e). By 10 min of treatment, the cell membrane shrinks more prominently (Fig. 5f). After 15 min, the cell wall was deformed with small evident pits, which demonstrated that some reactive oxygen species and thermal energy had been rapidly produced and acted on the surface of bacteria cells in the photodynamic inactivation process (Fig. 5g). At the end of the irradiation (Fig. 5h–i), almost the entire cell surface were destroyed with abundant pores. Undoubtedly, the *S.*

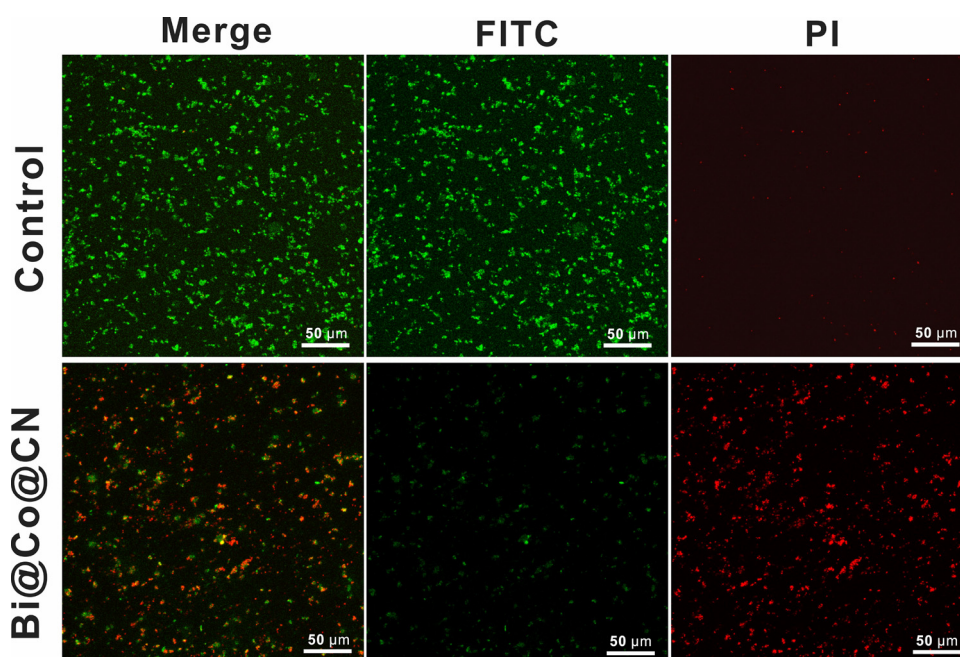


Fig. 4. Fluorescent images of live/dead *S. aureus*.

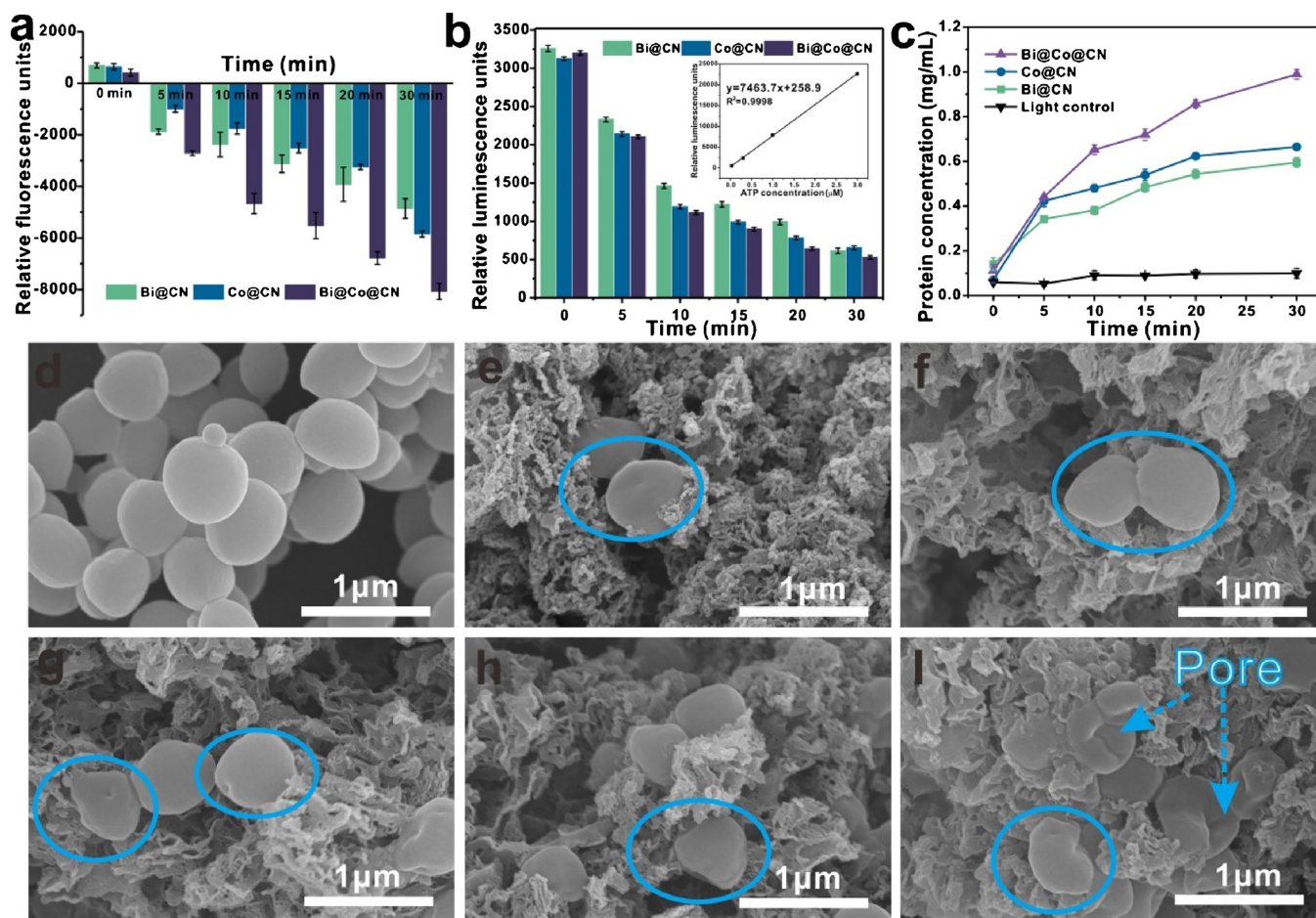


Fig. 5. (a) Effects of different samples against *S. aureus* on the membrane potentials. (b) Effects of different samples on intracellular ATP in *S. aureus*, which was represented by relative luminescence. (c) The total protein of *S. aureus* at time interval 0, 5, 10, 15, 20, 30 min. SEM images of *S. aureus* treated with Bi@Co@CN ($200 \mu\text{g mL}^{-1}$) under irradiation for (d) 0, (e) 5, (f) 10, (g) 15, (h) 20, (i) 30 min.

aureus cells were completely killed by Bi@Co@CN composites under visible-light irradiation. Therefore, it can be concluded that after photodynamic inactivation and photothermal disinfection, the integrity of the bacterial cells is severely disrupted, leading to the leakage of bacterial contents and eventually killing all bacteria [56–58].

3.4. Photodynamic inactivation on expression of bacterial virulence factors

Staphylococcus aureus is an opportunistic pathogen that can produce a variety of exotoxins, which contribute to its pathogenicity. It produces numerous exotoxins, such as enterotoxin A (SEA), coagulase, α -haemolysin, agr locus (agrA), and toxic shock syndrome toxin (TSST-1), which are involved in the infection of *S. aureus* pathogenesis [59,60]. Among these virulence factors, α -haemolysin is one of the most important exoproteins contributing to the haemolytic activity of *S. aureus* culture supernatants. Coagulase is also an important virulence factor of *S. aureus*, which protects pathogens from phagocytosis or from antibody binding. To determine their expression in photodynamic inactivation, haemolysis and coagulase titre assays were conducted. Fig. S11a shows that the Bi@Co@CN composite led to a significant inhibition of *S. aureus* haemolysis. At the same time, coagulase expression was also inhibited (Fig. S11b). To further determine the expression of virulence factors in the presence of Bi@Co@CN, SEA, TSST-1, agrA (i.e. the major enterotoxins of *S. aureus*), and α -haemolysin, the irradiated suspension of Bi@Co@CN were subjected to reverse transcription PCR (RT-PCR) analysis to detect their relative expression levels. The primer pairs used in RT-PCR were listed in Supplementary Table S3. As expected, the transcription levels of these genes were significantly reduced in the

ATCC 29,213 strain, proving that the expression level of these genes in *Staphylococcus aureus* was significantly inhibited by Bi@Co@CN under visible light irradiation (Fig. 6a–d). Furthermore, MRSA was selected to investigate the antibacterial ability, because it is resistant to a large group of antibiotics and poses a serious public health threat. Fig. 6e shows that MRSA bacteria were almost completely killed after 30 min of visible-light irradiation. The RT-PCR analysis showed that the methicillin-resistant gene (mecA) was inhibited during the photodynamic process (Fig. 6f). These findings revealed that our composite attacks both standard *S. aureus* and MRSA, and suggest that Bi@Co@CN could be used for the treatment of *S. aureus* infections by interfering with virulence factor expression.

3.5. In vivo assessment of wound healing

Biomedical applications of nanocomposites require demonstration of the stability of nanocomposites under physiological conditions and biocompatibility with mammalian cells [61,62]. To assess the activity *in vivo*, the photodynamic therapeutic efficacies of the different materials on wound healing were evaluated in animal models (Fig. 7a). The backs of Balb/c mice (8 weeks) were excised and injected with ca. 10^7 MRSA cells to construct an infected wound model. The mice were divided into four groups, variously treated with phosphate-buffered saline (PBS), Bi@CN, Co@CN, and Bi@Co@CN. No erythema appeared in the wounds treated with the Bi@Co@CN composite during the entire treatment process. Fig. 7b shows clear incrustation in the Bi@Co@CN group after 4 day of treatment. The incrustation formed by the coagulation of platelets, fibrin, and fibrinogen has a dual function, namely the

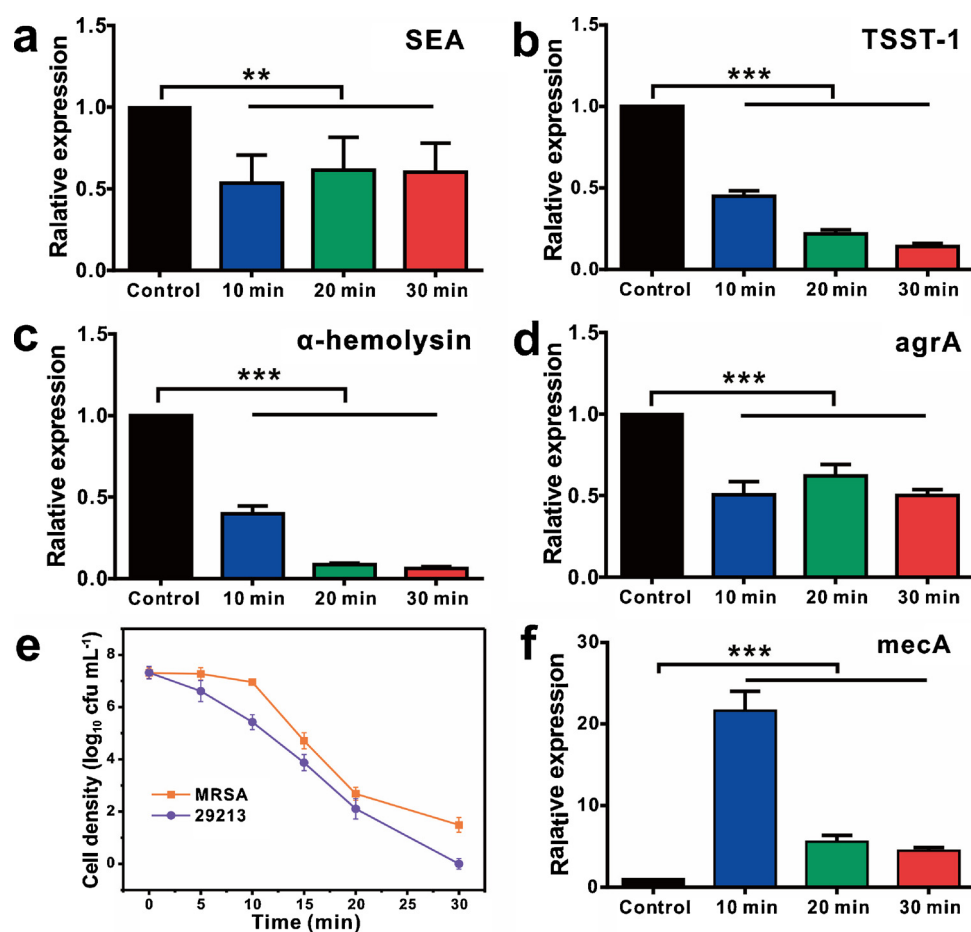


Fig. 6. (a) Expression the transcription of *S. aureus* SEA (a), TSST-1 (b), α -hemolysin (c), agrA (d). (e) Cell density of Bi@Co@CN against *S. aureus* 29,213 and MRSA under visible-light irradiation, respectively. (f) Expression the transcription of MRSA mecA.

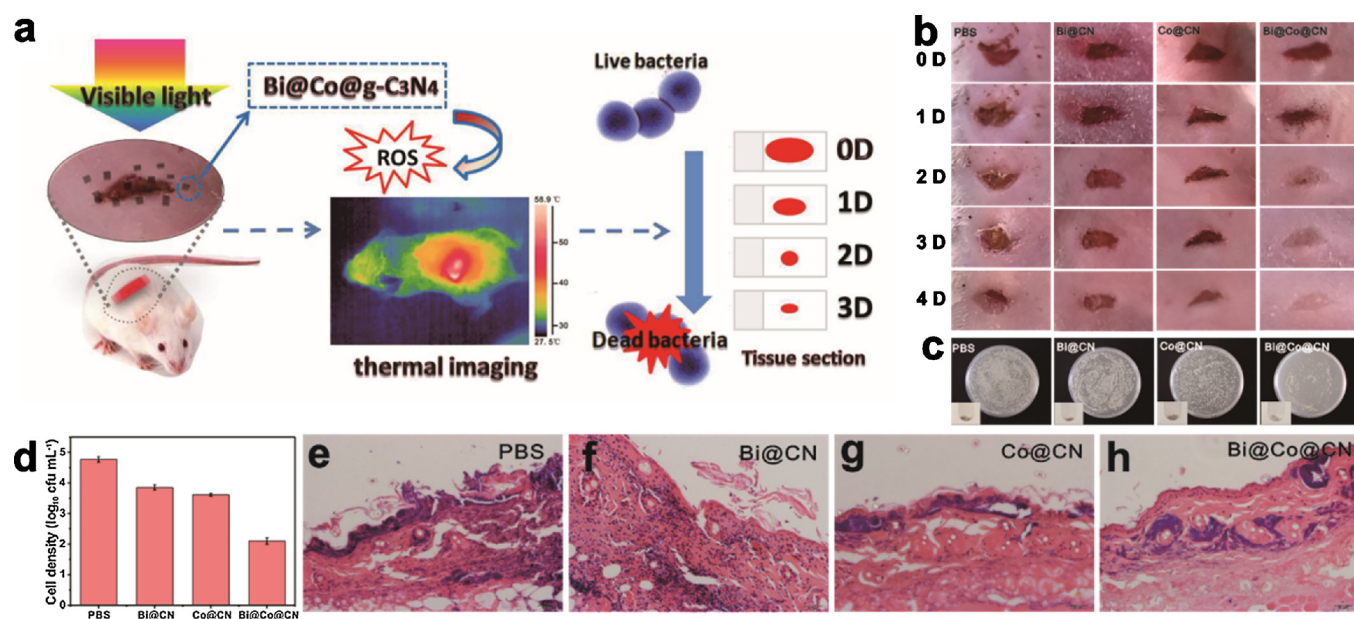


Fig. 7. (a) The concept of Bi@Co@CN photocatalyst as an efficient antimicrobial agent. (c) Photographs of wound on the mice during the therapeutic process. The mice samples were treated with PBS, Bi@CN, Co@CN, and Bi@Co@CN, respectively. (c) The bacteria isolated from wound tissue are cultured on agar plates. The insert is wound tissue. (d) Colony growth of wound tissue on LB agar plates. Photomicrographs showing section of skin tissues with H&E staining, treated with PBS (e), Bi@CN (f), Co@CN (g), and Bi@Co@CN (h), respectively.

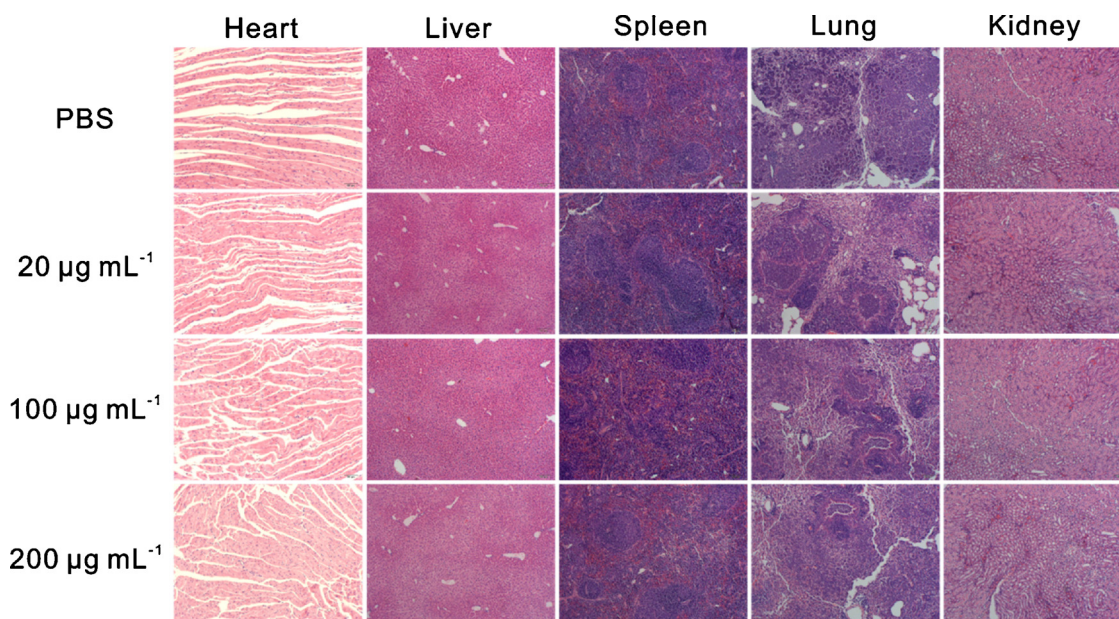


Fig. 8. The major organs (heart, liver, spleen, lung and kidney) after 4 days of treatment with an applied concentration of $20 \mu\text{g mL}^{-1}$, $100 \mu\text{g mL}^{-1}$, $200 \mu\text{g mL}^{-1}$ and PBS.

production of monomers that polymerise into fibrin, and acting as co-factor in platelet aggregation. The bactericidal effect was assessed by quantifying the amount of bacteria present in excised wound tissue (Fig. 7c–d). Colony growth revealed that Bi@Co@CN provided the most effective wound antimicrobial treatment. The control group was concurrently tested for infection treatment. Wound healing progression was evaluated by hematoxylin and eosin (H&E)-stained sectioning. Fig. 7e–h shows that after 4 days of treatment of the control group, a large number of inflammatory cells and flaky epidermal layers appeared on the wound, whereas the Bi@Co@CN group showed intact epidermal layers and fewer inflammatory cells. Therefore, it is concluded that Bi@Co@CN had the best antibacterial and wound healing performance among the various antibacterial agents tested.

Although the results strongly support excellent antibacterial performance of the Bi@Co@CN nanocomposite, the *in vivo* biosafety of the antibacterial system should also be considered. To evaluate the biocompatibility of Bi@Co@CN nanocomposite, MTT cytotoxicity assay was assessed using NIH 3T3 fibroblast cells [63,64]. For the MTT cytotoxicity assay (Fig. S12), cells were incubated with different concentrations of Bi@Co@CN for 24 h. Even at the highest concentration of $400 \mu\text{g mL}^{-1}$, 98% of the incubated cells remained viable after 24 h incubation, revealing a good bio-compatibility. Additionally, no significant abnormalities or damage to the major organs of mice (no infection) were observed even at 4 days after the injection of Bi@Co@CN at a concentration of $20 \mu\text{g mL}^{-1}$, $100 \mu\text{g mL}^{-1}$, and even at a high concentration of $200 \mu\text{g mL}^{-1}$ (Fig. 8). These results indicate that the side effects of this antibacterial agent in mice in the antibacterial treatment process are negligible. It is believed that metallic Bi and metallic Co promote $\text{g-C}_3\text{N}_4$ to produce a large number of ROS and thermal energy, which lead to synergistic antibacterial activity during wound healing [24,65–68]. Compared with the previous antibacterial agents, the main features of our antibacterial nanocomposites can be summarized as the following three points. First, this is the first report of using a multifunctional recyclable antibacterial nanocomposite for both photocatalytic and photothermal disinfection. Second, our nanocomposites exhibited greatly enhanced broad-spectrum antibacterial activity against most bacteria (including Gram-positive and Gram-negative bacteria) and MRSA compared with previous antimicrobials. Third, biocompatibility experiments showed that our composites are safe therapeutic materials for the treatment of bacterial infections.

These characteristics were solidly confirmed by *in vitro* and *in vivo* antibacterial experiments. Our research findings may pave the way for the evaluation of photodynamic materials as new antibacterial agents in clinical applications.

4. Conclusion

We demonstrated the efficient harvesting of visible light for photodynamic inactivation by a novel material, Bi@Co@CN. This nanocomposite exhibited faster photodynamic inactivation compared with most studied photocatalysts. This inactivation system demonstrated a broad and reusable antibacterial efficacy against both *S. aureus* 29,213 and MRSA through the generation of ROS and thermal energy under visible-light irradiation, inhibited the expression of virulence factors of *S. aureus*, and promoted wound healing accompanied by bacteria infections. Profiting from the efficient charge carrier separation and photothermal conversion, Bi@Co@CN can be served as an efficient light-harvesting catalyst for photodynamic inactivation in the practical application of wound healing.

Acknowledgements

This research was financed by National Natural Science Foundation of China (No. 21675127), the Shaanxi Provincial Science Fund for Distinguished Young Scholars (2018JC-011) and Capacity Building Project of Engineering Research Center of Qinghai Province (2017-GX-G03).

Appendix A. Supplementary data

Supplementary material related to this article can be found, in the online version, at doi:<https://doi.org/10.1016/j.apcatb.2018.09.030>.

References

- [1] S.Y. Tong, J.S. Davis, E. Eichenberger, T.L. Holland, V.G. Fowler Jr., *Staphylococcus aureus* infections: epidemiology, pathophysiology, clinical manifestations, and management, Clin. Microbiol. Rev. 28 (2015) 603–661.
- [2] Y. Liu, S.Y. Ding, R. Dietrich, E. Martlbauer, K. Zhu, A biosurfactant-inspired heptapeptide with improved specificity to kill MRSA, Angew. Chem. Int. Ed. 56 (2017) 1486–1490.

- [3] Y.Z.Y. Xie, Y. Liu, J.C. Yang, Y. Liu, F.P. Hu, K. Zhu, X.Y. Jiang, Gold nanoclusters for targeting methicillin-resistant *Staphylococcus aureus* in vivo, *Angew. Chem. Int. Ed.* 57 (2018) 3958–3962.
- [4] J.W. Alexander, History of the medical use of silver, *Surg. Infect.* 10 (2009) 289–292.
- [5] S. Chernousova, M. Epple, Silver as antibacterial agent: ion, nanoparticle, and metal, *Angew. Chem. Int. Ed.* 52 (2013) 1636–1653.
- [6] J. Wang, Q.F. Yang, L. Zhang, M.S. Liu, N. Hu, W.T. Zhang, W.X. Zhu, R. Wang, Y.R. Suo, J.L. Wang, A hybrid monolithic column based on layered double hydroxide-alginate hydrogel for selective solid phase extraction of lead ions in food and water samples, *Food Chem.* 257 (2018) 155–162.
- [7] R. Hirscha, T. Ternesa, K. Haberera, K.L. Kratzb, Occurrence of antibiotics in the aquatic environment, *Sci. Total Environ.* 225 (1999) 109–118.
- [8] J. Davies, Inactivation of antibiotics and the dissemination of resistance genes, *Science* 264 (1994) 375–382.
- [9] M. Zasloff, Antimicrobial peptides of multicellular organisms, *Nature* 415 (2002) 389–395.
- [10] W.J. Ong, L.L. Tan, Y.H. Ng, S.T. Yong, S.P. Chai, Graphitic carbon nitride (g-C₃N₄)-based photocatalysts for artificial photosynthesis and environmental remediation: are we a step closer to achieving sustainability? *Chem. Rev.* 116 (2016) 7159–7329.
- [11] M.Y. Ye, Z.H. Zhao, Z.F. Hu, L.Q. Liu, H.M. Ji, Z.R. Shen, T.Y. Ma, 0D/2D heterojunctions of vanadate quantum dots/graphitic carbon nitride nanosheets for enhanced visible-light-driven photocatalysis, *Angew. Chem. Int. Ed.* 56 (2017) 1–6.
- [12] M. Zhang, J. Xu, R.L. Zong, Y.F. Zhu, Enhancement of visible light photocatalytic activities via porous structure of g-C₃N₄, *Appl. Catal. B: Environ.* 147 (2014) 229–235.
- [13] S.L. Ma, S.H. Zhan, Y.G. Xia, P.F. Wang, Q.L. Hou, Q.X. Zhou, Enhanced photocatalytic bactericidal performance and mechanism with novel Ag/ZnO/g-C₃N₄ composite under visible light, *Catal. Today*. DOI:10.1016/j.cattod.2018.04.014.
- [14] L.Q. Jing, Y.G. Xu, S.Q. Huang, M. Xie, M.Q. He, H. Xu, H.M. Li, Q. Zhang, Novel magnetic CoFe₂O₄/Ag/Ag₃VO₄ composites: highly efficient visible light photocatalytic and antibacterial activity, *Appl. Catal. B: Environ.* 199 (2016) 11–22.
- [15] C.Y. Mao, Y.M. Xiang, X.M. Liu, Z.D. Cui, X.J. Yang, K.W.K. Yeung, H.B. Pan, X.B. Wang, P.K. Chu, S.L. Wu, Photo-inspired antibacterial activity and wound healing acceleration by hydrogel embedded with Ag/AgCl/ZnO nanostructures, *ACS Nano* 11 (2017) 9010–9021.
- [16] C. Liu, D. Kong, P.C. Hsu, H. Yuan, H.W. Lee, Y.Y. Liu, H.T. Wang, S. Wang, K. Yan, D.C. Lin, P.A. Maraccini, K.M. Parker, A.B. Boehm, Y. Cui, Rapid water disinfection using vertically aligned MoS₂ nanofilms and visible light, *Nat. Nanotech.* 11 (2016) 1098–1104.
- [17] R. Wang, X.Y. Kong, W.T. Zhang, W.X. Zhu, L.J. Huang, J. Wang, X. Zhang, X.N. Liu, N. Hu, Y.R. Suo, J.L. Wang, Mechanism insight into rapid photocatalytic disinfection of *Salmonella* based on vanadate QDs-interspersed g-C₃N₄ heterostructures, *Appl. Catal. B: Environ.* 225 (2018) 228–237.
- [18] K. Li, S.M. Gao, Q.Y. Wang, H. Xu, Z.Y. Wang, B.B. Huang, Y. Dai, J. Lu, In-situ-reduced synthesis of Ti³⁺ self-doped TiO₂/g-C₃N₄ heterojunctions with high photocatalytic performance under LED light irradiation, *ACS Appl. Mater. Interfaces* 7 (2015) 9023–9030.
- [19] K.C. Christoforidis, T. Montini, E. Bontempi, S. Zafeirotas, J.J.D. Jaén, P. Fornasiero, Synthesis and photocatalytic application of visible-light active β -Fe₂O₃/g-C₃N₄ hybrid nanocomposites, *Appl. Catal. B: Environ.* 187 (2016) 171–180.
- [20] G. Zhou, X.Y. Xu, J.Y. Yu, B. Feng, Y. Zhang, J.G. Hu, Y.X. Zhou, Vertically aligned MoS₂/MoO₃ heterojunction nanosheets for enhanced visible-light photocatalytic activity and photostability, *CrystEngComm* 16 (2014) 9025–9032.
- [21] Y. Shiraishi, Y. Kofuji, S. Kanazawa, H. Sakamoto, S. Ichikawa, S. Tanaka, T. Hirai, Platinum nanoparticles strongly associated with graphitic carbon nitride as efficient co-catalysts for photocatalytic hydrogen evolution under visible light, *Chem. Commun.* 50 (2014) 15255–15258.
- [22] L.B. Lv, T.N. Ye, L.H. Gong, K.X. Wang, J. Su, X.H. Li, J.S. Chen, Anchoring cobalt nanocrystals through the plane of graphene: highly integrated electrocatalyst for oxygen reduction reaction, *Chem. Mater.* 27 (2015) 544–549.
- [23] Z.W. Tong, D. Yang, Z. Li, Y.H. Nan, F. Ding, Y.C. Shen, Z.Y. Jiang, Thylakoid-inspired multishell g-C₃N₄ nanocapsules with enhanced visible-light harvesting and electron transfer properties for high-efficiency photocatalysis, *ACS Nano* 11 (2017) 1103–1112.
- [24] F. Dong, Z.W. Zhao, Y.J. Sun, Y.X. Zhang, S. Yan, Z.B. Wu, An advanced semimetal-organic Bi spheres-g-C₃N₄ nanohybrid with SPR-enhanced visible-light photocatalytic performance for NO purification, *Environ. Sci. Technol.* 49 (2015) 12432–12440.
- [25] X.C. Wang, K. Maeda, A. Thomas, K. Takanabe, G. Xin, J.M. Carlsson, K. Domen, M. Antonietti, A metal-free polymeric photocatalyst for hydrogen production from water under visible light, *Nat. Mater.* 8 (2009) 76–80.
- [26] H. Su, K.X. Zhang, B. Zhang, H.H. Wang, Q.Y. Yu, X.H. Li, M. Antonietti, J.S. Chen, Activating cobalt nanoparticles via the mott-schottky effect in nitrogen-rich carbon shells for base-free aerobic oxidation of alcohols to esters, *J. Am. Chem. Soc.* 139 (2017) 811–818.
- [27] G. Zhou, X.Y. Xu, T. Ding, B. Feng, Z.J. Bao, J.G. Hu, Well-steered charge-carrier transfer in 3D branched Cu₂O/ZnO@Au heterostructures for efficient photocatalytic hydrogen evolution, *ACS Appl. Mater. Interfaces* 7 (2015) 26819–26827.
- [28] J. Li, X.Y. Wu, W.F. Pan, G.K. Zhang, H. Chen, Vacancy-rich monolayer BiO_{2-x} as a highly efficient UV, visible, and near-infrared responsive photocatalyst, *Angew. Chem. Int. Ed.* 57 (2018) 491–495.
- [29] H. Li, F. Qin, Z.P. Yang, X.M. Cui, J.F. Wang, L.Z. Zhang, New reaction pathway induced by plasmon for selective benzyl alcohol oxidation on BiOCl possessing oxygen vacancies, *J. Am. Chem. Soc.* 139 (2017) 3513–3521.
- [30] Y. Cheng, Y. Chang, Y.L. Feng, H. Jian, Z.H. Tang, H.Y. Zhang, Deep-level defect enhanced photothermal performance of bismuth sulfide-gold heterojunction nanorods for photothermal therapy of cancer guided by computed tomography imaging, *Angew. Chem. Int. Ed.* 57 (2018) 246–251.
- [31] C. Zhang, Y.F. Zhu, Synthesis of square Bi₂WO₆ nanoplates as high-activity visible-light-driven photocatalysts, *Chem. Mater.* 17 (2005) 3537–3545.
- [32] X.C. Meng, Z.Z. Li, H.M. Zeng, J. Chen, Z.S. Zhang, MoS₂ quantum dots-interspersed Bi₂WO₆ heterostructures for visible light-induced detoxification and disinfection, *Appl. Catal. B: Environ.* 210 (2017) 160–172.
- [33] R.A. He, S.W. Cao, P. Zhou, J.G. Yu, Recent advances in visible light Bi-based photocatalysts, *Chin. J. Catal.* 35 (2014) 989–1007.
- [34] J. Ren, W.Z. Wang, S.M. Sun, L. Zhang, J. Chang, Enhanced photocatalytic activity of Bi₂WO₆ loaded with Ag nanoparticles under visible light irradiation, *Appl. Catal. B: Environ.* 92 (2009) 50–55.
- [35] X.H. Li, M. Antonietti, Metal nanoparticles at mesoporous N-doped carbons and carbon nitrides: functional Mott–Schottky heterojunctions for catalysis, *Chem. Soc. Rev.* 42 (2013) 6593–6604.
- [36] J.G. Yu, S.H. Wang, B. Cheng, Z. Lin, F. Huang, Noble metal-free Ni(OH)₂-g-C₃N₄ composite photocatalyst with enhanced visible-light photocatalytic H₂-production activity, *Catal. Sci. Technol.* 3 (2013) 1782–1789.
- [37] A.H. Lv, C. Hu, Y.L. Nie, J.H. Qu, Catalytic ozonation of toxic pollutants over magnetic cobalt and manganese co-doped γ -Fe₂O₃, *Appl. Catal. B: Environ.* 100 (2010) 62–67.
- [38] J. Li, G.X. Wang, Z.M. Xu, Environmentally-friendly oxygen-free roasting/wet magnetic separation technology for in situ recycling cobalt, lithium carbonate and graphite from spent LiCoO₂/graphite lithium batteries, *J. Hazard. Mater.* 302 (2016) 97–104.
- [39] I.A. Khan, Z.M. Mirza, A. Kumar, V. Verma, G.N. Qazi, Piperine, a phytochemical potentiator of ciprofloxacin against *Staphylococcus aureus*, *Antimicrob. Agents Chemother.* 50 (2006) 810–812.
- [40] F.D. Lowy, *Staphylococcus aureus* infections, *N. Engl. J. Med.* 339 (1998) 520–532.
- [41] H.X. Lin, W.H. Deng, T.H. Zhou, S.B. Ning, J.L. Long, X.X. Wang, Iodine-modified nanocrystalline titania for photo-catalytic antibacterial application under visible light illumination, *Appl. Catal. B: Environ.* 176–177 (2015) 36–43.
- [42] J. Li, Y.C. Yin, E.Z. Liu, Y.M. Ma, J. Wan, J. Fan, X.Y. Hu, In situ growing Bi₂MoO₆ on g-C₃N₄ nanosheets with enhanced photocatalytic hydrogen evolution and disinfection of bacteria under visible light irradiation, *J. Hazard. Mater.* 321 (2017) 183–192.
- [43] Y.N. Jia, S.H. Zhan, S.L. Ma, Q.X. Zhou, Fabrication of TiO₂-Bi₂WO₆ binanosheet for enhanced solar photocatalytic disinfection of *E. coli*: insights on the mechanism, *ACS Appl. Mater. Interfaces* 8 (2016) 6841–6851.
- [44] W.J. He, Y.J. Sun, G.M. Jiang, H.W. Huang, X.M. Zhang, F. Dong, Activation of amorphous Bi₂WO₆ with synchronous Bi metal and Bi₂O₃ coupling: photocatalysis mechanism and reaction pathway, *Appl. Catal. B: Environ.* 232 (2018) 340–347.
- [45] J.Y. Li, X.A. Dong, Y.J. Sun, W.L. Cen, F. Dong, Facet-dependent interfacial charge separation and transfer in plasmonic photocatalysts, *Appl. Catal. B: Environ.* 226 (2018) 269–277.
- [46] H. Wang, W.D. Zhang, X.W. Li, J.Y. Li, W.L. Cen, Q.Y. Li, F. Dong, Highly enhanced visible light photocatalysis and in situ FT-IR studies on Bi metal@defective BiOCl hierarchical microspheres, *Appl. Catal. B: Environ.* 225 (2018) 218–227.
- [47] G. Zhou, Y. Shan, Y.Y. Hu, X.Y. Xu, L.Y. Long, J.L. Zhang, J. Dai, J.H. Guo, J.C. Shen, S. Li, L.Z. Liu, X.L. Wu, Half-metallic carbon nitride nanosheets with micro grid mode resonance structure for efficient photocatalytic hydrogen evolution, *Nat. Commun.* 9 (2018) 3366.
- [48] D.H. Xia, Z.R. Shen, G.C. Huang, W.J. Wang, J.C. Yu, P.K. Wong, Red phosphorus: an earth-abundant elemental photocatalyst for "Green" bacterial inactivation under visible light, *Environ. Sci. Technol.* 49 (2015) 6264–6273.
- [49] R. Wang, W.T. Zhang, W.X. Zhu, L.Z. Yan, S.H. Li, K. Chen, N. Hu, Y.R. Suo, J.L. Wang, Enhanced visible-light-driven photocatalytic sterilization of tungsten trioxide by surface-engineering oxygen vacancy and carbon matrix, *Chem. Eng. J.* 348 (2018) 292–300.
- [50] W.T. Zhang, S. Shi, Y.R. Wang, S.X. Yu, W.X. Zhu, X. Zhang, D.H. Zhang, B.W. Yang, X. Wang, J.L. Wang, Versatile molybdenum disulfide based antibacterial composites for *in vitro* enhanced sterilization and *in vivo* focal infection therapy, *Nanoscale* 8 (2016) 11642–11648.
- [51] L. Sun, T. Du, C. Hu, J.N. Chen, J. Lu, Z.C. Lu, H.Y. Han, Antibacterial activity of graphene oxide/g-C₃N₄ composite through photocatalytic disinfection under visible light, *ACS Sustain. Chem. Eng.* 5 (2017) 8693–8701.
- [52] E. Sanchez, N. Heredia, R. Camacho-Corona Mdel, S. Garcia, Isolation, characterization and mode of antimicrobial action against *Vibrio cholerae* of methyl gallate isolated from *Acacia farnesiana*, *J. Appl. Microbiol.* 115 (2013) 1307–1316.
- [53] C. Shi, Y. Sun, Z.W. Zheng, X.R. Zhang, K.K. Song, Z.Y. Jia, Y.F. Chen, M.C. Yang, X. Liu, R. Dong, X.D. Xia, Antimicrobial activity of syringic acid against *Cronobacter sakazakii* and its effect on cell membrane, *Food Chem.* 197 (2016) 100–106.
- [54] K.L. Whiteaker, S.M. Gopalakrishnan, D.G.C.C. Shieh, U. Warrior, D.J. Burns, M.J. Coghlan, V.E. Scott, M. Gopalakrishnan, Validation of FLIPR membrane potential dye for high throughput screening of potassium channel modulators, *J. Biomol. Screen.* 6 (2001) 305–312.
- [55] E. Sanchez, S. Garcia, N. Heredia, Extracts of edible and medicinal plants damage membranes of *Vibrio cholerae*, *Appl. Environ. Microbiol.* 76 (2010) 6888–6894.
- [56] Y. Li, X.M. Liu, L. Tan, Z.D. Cui, X.J. Yang, Y.F. Zheng, K.W.K. Yeung, P.K. Chu, S.L. Wu, Rapid sterilization and accelerated wound healing using Zn²⁺ and graphene oxide modified g-C₃N₄ under dual light irradiation, *Adv. Fun. Mater.* 28 (2018) 1800299.
- [57] Q.Q. Yin, L.X. Tan, Q.Q. Lang, X.X. Ke, L.J. Bai, K.Y. Guo, R. Qiao, S. Bai, Plasmonic molybdenum oxide nanosheets supported silver nanocubes for enhanced near-

- infrared antibacterial activity: Synergism of photothermal effect, silver release and photocatalytic reactions, *Appl. Catal. B: Environ.* 224 (2018) 671–680.
- [58] D.H. Xia, W.J. Wang, R. Yin, Z.F. Jiang, T.C. An, G.Y. Li, H.J. Zhao, P.K. Wong, Enhanced photocatalytic inactivation of *Escherichia coli* by a novel Z-scheme g-C₃N₄/m-Bi₂O₄ hybrid photocatalyst under visible light: the role of reactive oxygen species, *Appl. Catal. B: Environ.* 214 (2017) 23–33.
- [59] J.Z. Qiu, H.H. Feng, J. Lu, H. Xiang, D.C. Wang, J. Dong, J.F. Wang, X.L. Wang, J.X. Liu, X.M. Deng, Eugenol reduces the expression of virulence-related exoproteins in *Staphylococcus aureus*, *Appl. Environ. Microbiol.* 76 (2010) 5846–5851.
- [60] G.H. Li, M.Y. Qiao, Y. Guo, X. Wang, Y.F. Xu, X.D. Xia, Effect of subinhibitory concentrations of chlorogenic acid on reducing the virulence factor production by *Staphylococcus aureus*, *Foodborne Pathog. Dis.* 11 (2014) 677–683.
- [61] F.F. Cao, E.G. Ju, Y. Zhang, Z.Z. Wang, C.Q. Liu, W. Li, Y.Y. Huang, K. Dong, J.S. Ren, X.G. Qu, An efficient and benign antimicrobial depot based on silver-infused MoS₂, *ACS Nano* 11 (2017) 4651–4659.
- [62] C.Y. Mao, Y.M. Xiang, X.M. Liu, Z.D. Cui, X.J. Yang, Z.Y. Li, S.L. Zhu, Y.F. Zheng, K.W.K. Yeung, S.L. Wu, Repeatable photodynamic therapy with triggered signaling pathways of fibroblast cell proliferation and differentiation to promote bacteria-accompanied wound healing, *ACS Nano* 12 (2018) 1747–1759.
- [63] R.F. Landis, C.H. Li, A. Gupta, Y.W. Lee, M. Yazdani, N. Ngernyuang, I. Altinbasak, S. Mansoor, M.A.S. Khichi, A. Sanyal, V.M. Rotello, Biodegradable nanocomposite antimicrobials for the eradication of multidrug-resistant bacterial biofilms without accumulated resistance, *J. Am. Chem. Soc.* 140 (2018) 6176–6182.
- [64] M.S. Liu, J. Wang, Q.F. Yang, N. Hu, W.T. Zhang, W.X. Zhu, R. Wang, Y.R. Suo, J.L. Wang, Patulin removal from apple juice using a novel cysteine-functionalized metal-organic framework adsorbent, *Food Chem.* 270 (2019) 1–9.
- [65] J.J. Wang, L. Tang, G.M. Zeng, Y.N. Liu, Y.Y. Zhou, Y.C. Deng, J.J. Wang, B. Peng, Plasmonic Bi metal deposition and g-C₃N₄ coating on Bi₂WO₆ microspheres for efficient visible-light photocatalysis, *ACS Sustain. Chem. Eng.* 5 (2016) 1062–1072.
- [66] G.M. Jiang, X.W. Li, M.N. Lan, T. Shen, X.S. Lv, F. Dong, S. Zhang, Monodisperse bismuth nanoparticles decorated graphitic carbon nitride: enhanced visible-light-response photocatalytic NO removal and reaction pathway, *Appl. Catal. B: Environ.* 205 (2017) 532–540.
- [67] L. Zhou, L.Z. Wang, J.Y. Lei, Y.D. Liu, J.L. Zhang, Fabrication of TiO₂/Co-g-C₃N₄ heterojunction catalyst and its photocatalytic performance, *Catal. Commun.* 89 (2017) 125–128.
- [68] N. Zhao, L.L. Kong, Y.M. Dong, G.L. Wang, X.M. Wu, P.P. Jiang, Insight into the crucial factors for photochemical deposition of cobalt cocatalysts on g-C₃N₄ photocatalysts, *ACS Appl. Mater. Interfaces* 10 (2018) 9522–9531.